SPECIAL
DYNAMO/CINDY/AMIE/LASP
COLLECTION

Atmospheric Overturning across Multiple Scales of an MJO Event during the CINDY/DYNAMO Campaign

XINGCHAO CHEN AND OLIVIER M. PAULUIS

Center for Prototype Climate Modeling, New York University Abu Dhabi, Abu Dhabi, United Arab Emirates, and Courant Institute of Mathematical Sciences, New York University, New York, New York

FUQING ZHANG

Department of Meteorology and Atmospheric Science, and Center for Advanced Data Assimilation and Predictability Techniques, The Pennsylvania State University, University Park, Pennsylvania

ABSTRACT

This study investigates the atmospheric overturning of the October 2011 MJO event observed during the Cooperative Indian Ocean Experiment on Intraseasonal Variability in the Year 2011 (CINDY)/DYNAMO field experiment using a cloud-permitting numerical model. The isentropic analysis is used to sort the vertical mass transport in terms of the equivalent potential temperature of the air parcels, which naturally decomposes the atmospheric overturning between ascending air with high entropy and subsiding air with low entropy. The circulation is further decomposed into contributions of four main scales: basinwide ascent, meridional overturning, regional overturning, and convection. Results show that the convective scale dominates the upward mass transport while larger scales play an important role both by allowing a deeper overturning and by modulating convective activity. There are substantial changes in the atmospheric overturning during different phases of this MJO event. Increased convective activity at low levels precedes the onset of the MJO by several days. The initiation of the MJO itself is associated with a substantial increase in the atmospheric overturning over the Indian Ocean. The subsequent eastward propagation of the MJO event can be clearly captured by the evolutions of convective-scale vertical mass fluxes at different altitudes. The equivalent potential temperatures of the rising and subsiding air parcels in the convective-scale overturning are also increased in the troposphere during the active phase of the MJO.

1. Introduction

The Madden–Julian oscillation (MJO; Madden and Julian 1971), with a period of 20–100 days, is the dominant component of intraseasonal variability in the tropical atmosphere (Majda and Biello 2004; Zhang 2005). Atmospheric overturning in the MJO is organized over a broad range of spatial and temporal scales within a large-scale envelope (predominantly of zonal wavenumber 2) that propagates eastward at an average speed of $5\,m\,s^{-1}$ across the warm waters of the Indian Ocean and the Western Pacific (Hendon and Liebmann 1994; Majda et al. 2007; Chen et al. 2014). The MJO exerts pronounced influences on monsoon systems, tropical cyclogenesis, El Niño, and the Southern Oscillation and has broad impacts on global climate and weather systems around the globe (Tyrrell et al. 1996; Bergman et al. 2001; Maloney and Hartmann 2001; Zhang 2005; Lorenz and Hartmann 2006; He et al. 2011; Pai et al. 2011; Klotzbach 2014; Chi et al. 2015). Though the MJO is a major source of intraseasonal predictability and has prominent impacts on climate, it is still an unmet challenge for global climate models to simulate and predict accurately (Slingo et al. 1996; Lin et al. 2006; Hung et al. 2013; Jiang et al. 2015). This difficulty exposes a gaping hole in our knowledge of tropical dynamics and, in particular, of the interactions between convection and atmospheric motions at larger scales (Zhang 2005; Zhang et al. 2013). The purpose of this paper is to diagnose the atmospheric overturning associated with a MJO event, to assess the contributions of the various scales of motions, and ultimately to seek better understanding of the multiscale interactions that are driving the MJO.

ⓐ Denotes content that is immediately available upon publication as open access.

Corresponding author: Xingchao Chen, xc18@nyu.edu

The international field campaign Cooperative Indian Ocean Experiment on Intraseasonal Variability in the Year 2011 (CINDY)/Dynamics of the Madden–Julian Oscillation (DYNAMO) was conducted in and around the tropical Indian Ocean from October 2011 to March 2012. Three MJO events (the October, November, and December MJO events) were captured by the sounding, ground-based radar, ship/mooring, and airborne (aircraft did not sample the October event) observational networks during the field campaign (Yoneyama et al. 2013; Zhang et al. 2013). A number of studies documented various aspects of these MJO events based on the collected in situ observations. For example, Johnson and Ciesielski (2013) diagnosed the large-scale kinematic and thermodynamic properties of the October and November MJO events based on the sounding array observations. Using shipborne radar, Xu and Rutledge (2014) investigated the convective population and atmospheric conditions over the central Indian Ocean in the three MJO events. Rowe and Houze (2014) compared the microphysical characteristics of convective systems observed by the dual-polarimetric Doppler S-band radar between the MJO active and inactive phases during October, November, and December. Using the same dual-polarimetric radar observations, Barnes and Houze (2014) also studied the microphysical characteristics of mature near-equatorial oceanic mesoscale convective systems during the MJO active phases. Moum et al. (2014) analyzed the air–ocean interactions from westerly wind burst in the November MJO event based on research vessel observations. The budget of moist static energy of the three MJO events was analyzed by Sobel et al. (2014) with the sounding array data.

Besides these observational studies, forecasting and simulating skills of global and regional models on the MJO events observed during CINDY/DYNAMO have also been examined in a variety of research works (Fu et al. 2013; Kerns and Chen 2014; Ling et al. 2014; Takemi 2015; S. Wang et al. 2015, hereinafter W15; W. Wang et al. 2015; Xiang et al. 2015; Hagos et al. 2016; Janiga and Zhang 2016; Pilon et al. 2016; Powell 2016). W15 simulated the October and November MJO events using a convection-permitting regional model with 9-km grid spacing. The authors compared the simulated atmospheric circulation, rainfall intensity and propagation, precipitable water, wavenumber-frequency distributions of surface precipitation, radiative fluxes, and the budget of moist static energy with multiple observational datasets. It is shown that the model successfully captured many aspects of the two simulated MJO events, especially for the October MJO event. In particular, the evolutions of large-scale circulation, the convective activity, and the cloud–radiative feedback, which are important to the MJO dynamics (Wang et al. 2016), are faithfully reproduced in the simulation.

The main objective of this study is to assess the variations in the atmospheric overturning of the MJO using convection-permitting simulations as in W15. While the convective mass transport can be easily obtained in a general circulation model owing to its reliance on convective parameterization, a particular challenge in using a high-resolution model lies in assessing the mass transport and the contribution of individual scales as the model simulates a broad range of motions. In this study, we apply the isentropic analysis framework introduced by Pauluis and Mrowiec (2013) in which the vertical mass transport is sorted out in terms of the equivalent potential temperature of the air parcels. This technique has the advantages of 1) identifying the atmospheric overturning associated with upward transport of warm moist air and downward transport of colder dryer air and 2) systematically filtering gravity waves. Vertical mass transport contributed by different scales of motions can thus be more easily identified (Slawinska et al. 2016). In this study, we systematically apply the isentropic analysis to investigate the evolution of the atmospheric overturning during the October MJO event using the same simulations as in W15. The experimental setup and analysis methodology are described in section 2. Section 3 analyzes the atmospheric mass transport associated with multiple scales. As mentioned above, the actual behavior of MJO is complex owing to a wide range of scales involved. Time filtering is usually needed to be applied to precipitation or OLR observations to capture the eastward propagation of the MJO. In this study, the eastward propagation of the MJO as an envelope of the convective-scale overturning characterized by isentropic analysis will be discussed in section 4 to see if this technique can capture the propagation of the MJO without any time filtering. This approach allows us not only to assess the evolution of convective mass transport over different subregions but also to assess the changes in the thermodynamic properties of the updrafts and downdrafts. Section 5 gives the concluding remarks of the study.

2. Experimental setup and methodology

a. WRF Model setup

The model configuration here is the same as the one used in W15. The Advanced Research version of WRF (Skamarock et al. 2008), version 3.4.1, is used to simulate the atmosphere over the whole equatorial Indian Ocean, from 20°S to 20°N and from 48° to 120°E (Fig. 1). The horizontal grid spacing is 9 km and there are 45 vertical levels with 9 levels in the lowest 1 km and a nominal top at 20 hPa. Vertically propagating gravity waves have been suppressed in the top 5 km of the model with
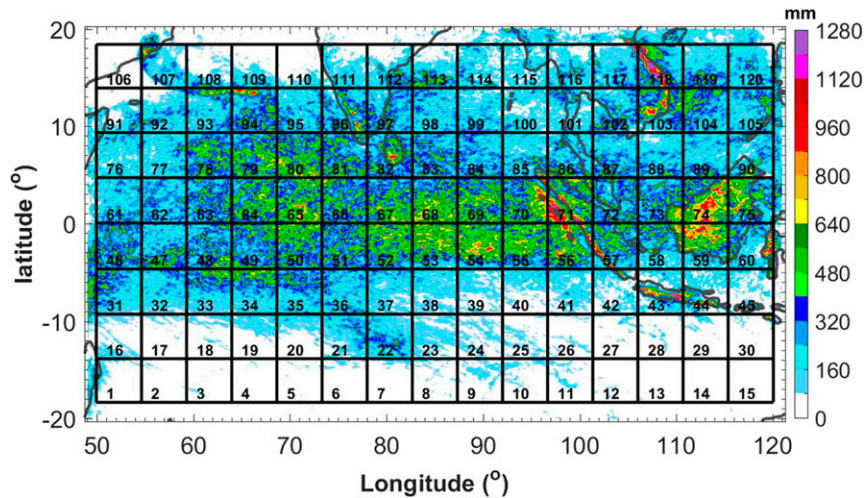
FIG. 1. Spatial distribution of the accumulated rainfall in the WRF simulation (color shading; from 4 Oct to 14 Nov 2011). Different subregions (450 km × 450 km) are indicated by the black rectangles. Coastlines are shown by the gray lines.

the implicit damping scheme (Klemp et al. 2008). The 6-hourly ERA-Interim (Dee et al. 2011) is used as the initial and boundary conditions for the WRF simulation, and SST is updated every 6 h using the ERA-Interim SST data. The simulation employs the unified Noah land surface physical scheme (Tewari et al. 2004), the Yonsei University (YSU) boundary layer scheme (Hong et al. 2006), the GCM version of the Rapid Radiative Transfer Model (RRTMG) longwave radiation scheme (Iacono et al. 2008), and the updated Goddard shortwave scheme (Shi et al. 2010). The WRF double-moment (WDM) microphysics scheme (Lim and Hong 2010) from WRF3.5.1 with an update on the limit of the shape parameters and terminal speed of snow is used in this simulation. No cumulus scheme has been used. The model integration starts from 0000 UTC 1 October 2011. For the first 3 days, a spectral nudging is used to relax the horizontal wind with a zonal wavenumber 0–4 and a meridional wavenumber 0–2, which constrains the large-scale flow and convergence in the domain and allows the mesoscale to saturate in the spectral space. More details on the model configurations and descriptions can be found in W15.

The simulation is integrated until 14 November 2011 without any further nudging after the first 3 days. The analysis focuses on the free run period from 4 October to 14 November. Figure 2 shows the Hovmöller diagrams of the 3-hourly rainfall averaged between the equator and 4.5°N from the WRF simulation and the TRMM observation. The WRF simulation reproduces both the intensity and the propagation of the surface rainfall, as previously discussed in W15. The observation and simulation clearly show that the October MJO event is initiated in the western Indian Ocean (~60°E) around

14 October (shown by the red dashed line) and propagates eastward with a speed around 5 m s^{-1}. The eastward propagation is disrupted near the Maritime Continent (~100°E) around 6 November (disrupted date herein). We also observe a westward propagation for each rainfall episode within the MJO envelope, which may be related to the propagations of equatorial Rossby waves and mixed Rossby–gravity waves (Wheeler and Kiladis 1999; Zuluaga and Houze 2013). The simulated surface rainfall intensity of several episodes is slightly stronger than that in the TRMM observations, while the WRF simulation captures the mean strength of these westward-propagating episodes. Precipitation over the Maritime Continent is little influenced by the MJO event, and a prominent diurnal cycle of precipitation is evident over Indonesia and Borneo. More details on the atmospheric environment and energy budgets of this MJO event can be found in W15.

b. Isentropic analysis

The isentropic analysis technique developed by Pauluis and Mrowiec (2013) is applied in this study to investigate the mean properties of atmospheric overturning across multiple scales during this MJO event. The isentropic analysis relies on sorting the vertical mass transport in terms of the equivalent potential temperature θ_e of air parcels and computes the atmospheric overturning in isentropic coordinates (z, θ_e). Compared with the Eulerian analysis, isentropic analysis filters out reversible oscillatory motions associated with gravity waves and emphasizes the fact that the vertical mass transport in convection (Pauluis and Mrowiec 2013; Pauluis 2016; Slawinska et al. 2016), mesoscale systems

(Mrowiec et al. 2012, 2015, 2016), and global atmospheric circulations (Pauluis et al. 2008, 2010; Yamada and Pauluis 2016) are all due to the combinations of ascending air parcels with high entropy and descending air parcels with low entropy.

The isentropic distribution of vertical mass transport on a given isentropic slice is defined as

$$\langle \rho W \rangle (z, \theta_{e0}) = \frac{1}{P L_x L_y} \int_0^P \int_0^{L_y} \int_0^{L_x} \rho W(x, y, z, t)$$
$$\times \delta[\theta_{e0} - \theta_e(x, y, z, t)] \, dx \, dy \, dt. \quad (1)$$

Here, ρ is the mass per unit volume, W is the vertical velocity, P is the time period over which the averaging is performed, L_x and L_y are the spatial extent of the averaging domain, and $\delta[\theta_{e0} - \theta_e(x, y, z, t)]$ is a Dirac function which is approximated here by a function that is equal to $1/\Delta\theta_e$ for θ_e between $\theta_{e0} - 0.5\Delta\theta_e$ and $\theta_{e0} + 0.5\Delta\theta_e$ and 0 elsewhere. In practice, the integral in (1) amounts to summing the vertical mass flux of air parcels at each constant height in finite θ_e bins on an interval of width $\Delta\theta_e$. In addition, θ_{e0} is the mean equivalent potential temperature of the finite bin and the isentropic integral $\langle \rho W \rangle$ is expressed in units of ρW per kelvin. The equivalent potential temperature θ_e is defined following Pauluis (2016)'s Eq. (2):

$$\left(C_{pd} + C_i r_T \right) \ln \frac{\theta_e}{T_f} = \left[C_{pd} + r_i C_i + (r_v + r_l) C_l \right] \ln \left(\frac{T}{T_f} \right) - R_d \ln \left(\frac{P_d}{P_0} \right) + (r_v + r_l) \frac{L_f}{T_f} + r_v \frac{L_v}{T} - r_v R_v \ln H, \quad (2)$$

where r_i, r_l, r_v, and r_T represent the mixing ratios for ice, liquid water, water vapor, and total water; C_i, C_l and C_{pd} are the specific heat capacities at constant pressure of ice, liquid water and dry air; R_v and R_d stand for the specific gas constants for water vapor and dry air; L_f and L_v are the latent heat of freezing and vaporization; H is the relative humidity; P_0 ($=1000$ hPa) and P_d are the reference pressure and partial pressure of dry air; and T_f ($=273.1$ K) and T are the freezing temperature for water under atmospheric pressure and temperature. From a physical point of view, this definition of θ_e would be the temperature of an air parcel that has been first expanded adiabatically to 0 hPa, then compressed back to the reference pressure of 1000 hPa while imposing that all the water remains in the ice phase. It is typically warmer by a few degrees than the definition of Emanuel (1994) and its primary advantage lies in that freezing of liquid water is not a source of θ_e, and, when used in the isentropic analysis, makes it easier to capture the deep convective overturning motions above the freezing level because its inclusion of the latent heat of freezing.

The isentropic distribution of vertical mass transport defined by Eq. (1) can be further integrated to obtain the following isentropic streamfunction:

$$\Psi(z, \theta_{e0}) = \int_0^{\theta_{e0}} \langle \rho W \rangle (z, \theta_e') \, d\theta_e'. \quad (3)$$

The isentropic streamfunction is equal to the net vertical mass flux of all air parcels with an equivalent potential temperature less than θ_{e0} at each height level z. Physically, it shows the averaged trajectory of all air parcels with similar equivalent potential temperature. Interested readers can also refer to Pauluis and Mrowiec (2013) for a more

detailed physical interpretation of the isentropic streamfunction.

c. Multiscale decomposition of mass flux

In this study, we separate the atmospheric overturning into different scales. First, we divide the WRF domain into 120 subregions (shown by the black rectangles in Fig. 1; 15 subregions in zonal and 8 subregions in meridional directions). The size of each subregion is 50×50 grid points, which is approximately 450 km $\times$ 450 km (we use here a Mercator grid, with a spatial spacing proportional to the cosine of the latitude). Isentropic analyses using different subregion sizes have been compared with each other and the results are shown to be not sensitive to the small changes of the subregion size (not shown here). At each model output time (hourly) and in each subregion, the vertical mass flux is decomposed into a convective component (ρW_C) and a large-scale component ($\bar{\rho} W_{LS}$):

$$\rho w = \rho W_C + \bar{\rho} W_{LS}(i, j). \quad (4)$$

The latter is calculated by averaging the vertical mass flux of all grid points in the subregion:

$$\bar{\rho} W_{LS}(i, j) = \frac{1}{A(i, j)} \iint \rho w a^2 \cos\phi \, d\phi \, d\lambda. \quad (5)$$

Here, $A(i, j)$ is the area of the corresponding subregion, $\bar{\rho}$ is the horizontal-mean mass per unit volume for each subregion, a is Earth's radius (6371 km), ϕ is the latitude, and λ is the longitude. The large-scale mass flux is further decomposed into a basinwide ascent ($\bar{\rho} W_B$), meridional overturning ($\bar{\rho} W_M$), and regional overturning ($\bar{\rho} W_R$) defined below:
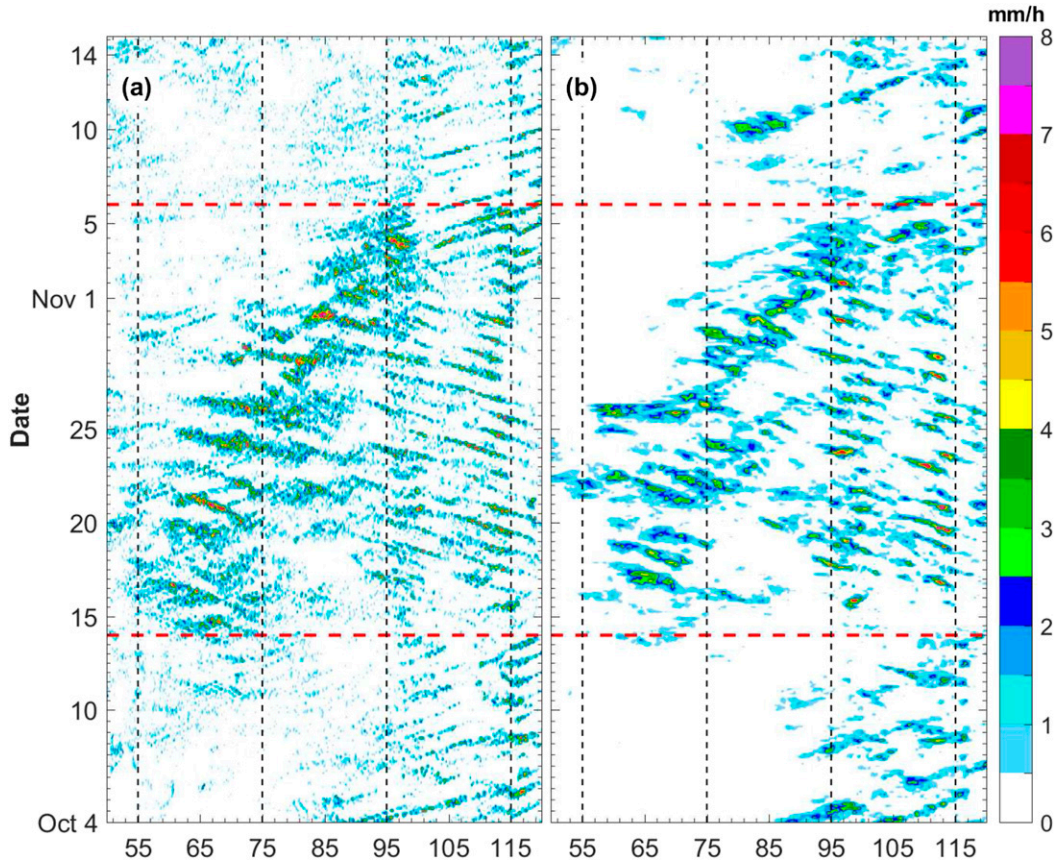
FIG. 2. Hovmöller diagrams of 3-hourly surface precipitation from (a) the WRF simulation and (b) TRMM observations averaged over latitudes 0°–4.5°N. The onset (14 Oct) and disrupted (6 Nov) date of the MJO event are shown by the red dashed lines. The black dashed lines are longitude grid lines.

$$\overline{\rho}W_B = \frac{1}{\displaystyle\sum_{j=1}^{NY}\sum_{i=1}^{NX} A(i,j)} \sum_{j=1}^{NY}\sum_{i=1}^{NX} \left[\overline{\rho}W_{LS}(i,j)A(i,j)\right], \quad (6)$$

$$\overline{\rho}W_M(j) = \frac{1}{\displaystyle\sum_{i=1}^{NX} A(i,j)} \sum_{i=1}^{NX} \left[\overline{\rho}W_{LS}(i,j) - \overline{\rho}W_B\right]A(i,j), \quad (7)$$

and

$$\overline{\rho}W_R(i,j) = \overline{\rho}W_{LS}(i,j) - \overline{\rho}W_B - \overline{\rho}W_M(j). \quad (8)$$

In the equations, NX = 15 and NY = 8 represent the number of subregions in the zonal and meridional directions. With these definitions, $\overline{\rho}W_B$ is the mean vertical mass flux over the whole model domain and accounts for basinwide ascending or descending motion, and $\overline{\rho}W_M$ shows the zonally averaged vertical mass transport beyond the basinwide overturning and accounts for the atmospheric overturning across different latitudes in this MJO event. Because the size of each subregion is

close to the spatial scale of organized convective systems (like squall lines), $\overline{\rho}W_R$ represents the characteristics of vertical mass transports associated mesoscale processes (regional scale). Additionally, ρW_C is the mass flux at each grid point after subtracting atmospheric overturning associated with basin, meridional, and regional scales; it stands for the vertical mass transport produced by the convective-scale activity. Using definitions in section 2b, the isentropic streamfunctions associated with basin (Ψ_B), meridional (Ψ_M), regional (Ψ_R), and convective (Ψ_C) scales are determined by Eq. (3). Thus, the total streamfunction Ψ is decomposed into

$$\Psi(z,\theta_{e0}) = \Psi_B(z,\theta_{e0}) + \Psi_M(z,\theta_{e0}) \\ + \Psi_R(z,\theta_{e0}) + \Psi_C(z,\theta_{e0}). \quad (9)$$

3. Atmospheric overturning across multiple scales

This section studies the multiscale atmospheric overturning in the October MJO event as described by the isentropic analysis. Figure 3 shows the isentropic

streamfunctions associated with multiple scales averaged over all 120 subregions from 4 October to 14 November 2011. Figure 3a shows the convective-scale isentropic streamfunction. The solid black line is the horizontal-mean profile of equivalent potential temperature. Because air parcels with low θ_e are on average subsiding in convection, given the definition of Eq. (3), the convective-scale streamfunction at each given height are first decreasing with θ_e. The vertical mass flux changes from negative to positive when the streamfunction reaches its minimum value at each level. The streamfunction is negative throughout the troposphere, indicating that the rising air parcels have higher θ_e than the subsiding air parcels on average which leads to a net upward transport of θ_e for the summed convective-scale circulation. In the streamfunction, isolines associated with deep convective drafts connect the surface with the upper troposphere (shown by the black dashed contour in Fig. 3a). The equivalent potential temperature θ_e of air parcels being lifted by deep convection drops from near the surface to the melting level (around 6 km), which is due to the entrainment of drier air in the updrafts. Above the melting level, the streamlines are almost vertical, reflecting that deep convective updraft can transport mass and energy upward without significant dilution above the freezing level. From the upper troposphere to the surface, the averaged potential temperature of the subsiding air parcels surrounding deep convective updrafts (shown by the left part of the black dashed contour in Fig. 3a) first decrease by 25 K from 14 to 1.5 km, which is induced by the radiative cooling effect, then increase by 15 K in the lowest 1.5-km level, which is closely related to the mixing between the subsiding environmental air and the detrained cloudy air that has a higher θ_e (Pauluis and Mrowiec 2013). When compared with the deep convective overturning that can transport mass from the surface to the upper troposphere, shallow convective-scale overturning is much more prominent (around one order magnitude greater) in the convective-scale streamfunction with a center located around 1–3 km and a top below 5 km (or melting level). It corresponds to the fact that shallow convective overturning dominates the mass transport in lower troposphere and produces the most precipitation over the tropical Indian Ocean (Liu et al. 2008). In shallow convective overturning, the θ_e of the air parcels is much higher than the mean profile of θ_e ($\sim$10 K), which shows air parcels in shallow cumulus are much warmer and moister than the environment [refer to Pauluis and Mrowiec (2013)].

The regional-scale isentropic streamfunction is presented in Fig. 3b, which indicates the collective contribution of organized mesoscale convective systems to the whole atmospheric overturning in this MJO event. When compared with the convective-scale streamfunction, the regional-scale streamfunction is shallower in the vertical and wider in the lower troposphere, which corresponds to weaker vertical motions at this scale. The isolines of the regional-scale streamfunction are closely aligned with the horizontal-mean profile of θ_e, showing the bulk of the regional-scale descending motions occurs at θ_e closer to the horizontal-mean atmospheric state than that of the convective-scale overturning. In the subsiding part of the regional-scale streamfunction, with slower vertical motions, both the reduction of θ_e above 1.5 km induced by the radiative cooling and the increase of θ_e in the lowest 1.5 km due to the mixing with detrained cloudy air are more prominent than those in the convective-scale streamfunction, which are 32 and 26 K, respectively. The regional-scale streamfunction peaks at around 4–9 km, which might correspond to the distinctive overturning in the anvil clouds that usually exist at the rear of mesoscale systems extending hundreds of kilometers (DePasquale et al. 2014; Slawinska et al. 2016).

Figure 3c shows the isentropic streamfunction associated with the meridional overturning over the Indian Ocean. The Hadley circulation is associated with ascending motions over the equatorial ITCZ and descending motion in the subtropics. When diagnosed through the isentropic streamfunction, the Hadley circulation shows up as rising motion of warm, moist air and subsiding motion of colder dryer air. Compared to the regional-scale counterpart, the streamfunction associated with the meridional scale is 1–2 km shallower, which reflects that the averaged depth of the meridional circulation is shallower than that of the organized mesoscale convective systems. The tilt of the streamfunction in the lower troposphere is also more prominent in the meridional-scale circulation, which indicates that the impacts of entrainment are stronger within the meridional circulation, which may be related to weaker vertical motions at this scale. The minimum of the meridional-scale streamfunction is located around 6 km, showing that the vertical mass transport of the meridional circulation is strongest in the middle troposphere.

Figure 3d shows the isentropic streamfunction associated with the basin scale. The dashed black line is the lowest θ_e above which the streamfunction is constant for each height level. The basin-scale streamfunction differs from those associated with other scales in that it does not vanish at high θ_e and therefore does not have a closed contour. This arises from the fact that the large-scale boundary conditions used in the simulations impose large-scale ascent over the entire basin, which is compensated by subsidence outside of the simulated domain.
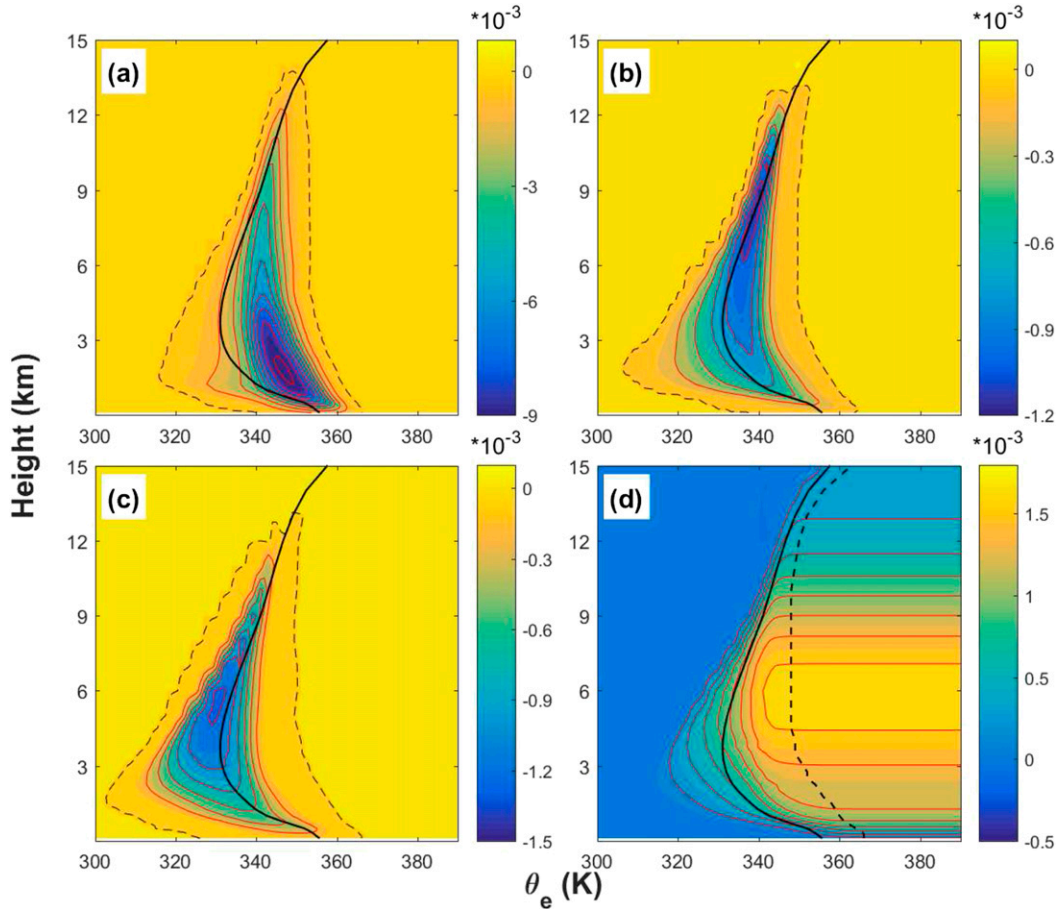
FIG. 3. Isentropic streamfunctions (color shading; $kg\,m^{-2}\,s^{-1}$) associated with the (a) convective scale, (b) regional scale, (c) meridional scale, and (d) basin scale averaged over 120 subregions from 4 Oct to 14 Nov 2011. The x axis is equivalent potential temperature (K) and the y axis is height (km). The black solid line shows the horizontal-mean profile of equivalent potential temperature averaged over 120 subregions. Isolines of stream-function are shown as red contours with a $-0.001\,kg\,m^{-2}\,s^{-1}$ interval in (a) and a $-0.0002\,kg\,m^{-2}\,s^{-1}$ interval in (b)–(d). The black dashed lines in (a)–(c) show the isolines of $0\,kg\,m^{-2}\,s^{-1}$. The black dashed line in (d) shows the lowest θ_e above which the basin-scale streamfunction is constant for each height level.

Similar to the meridional scale, the basin-scale stream-function also peaks around 6 km.

To further elucidate the temporal evolutions of the vertical mass transports across multiple scales, an isen-tropic upward mass transport is defined below following Slawinska et al. (2016)'s Eq. (10):

$$M(z) = \max_{\theta_e}\left[\Psi(z, \theta_{e0})\right] - \min_{\theta_e}\left[\Psi(z, \theta_{e0})\right]. \quad (10)$$

The maximum and minimum in Eq. (10) are taken for all values of θ_e at a fixed height. The evolution of the is-entropic mass transport associated with different scales is shown in Fig. 4. Black dashed lines show the active phase of the October MJO event (14 October–6 November), which corresponds to a substantial en-hancement of the atmospheric overturning over the entire region (Fig. 4a). This increase in overturning is primarily associated with an increase in the contribution by the convective overturning (Fig. 4b), albeit contributions from the meridional and basinwide overturning (Figs. 4d and 4e) are important in the middle to upper tropo-sphere. In contrast, contribution from the regional-scale circulation is relatively small (Fig. 4c) while an en-hancement can still be found at the end of the MJO event, which can be largely attributed to overturning in anvil clouds. This is because extensive stratiform regions are more common at the end of MJO events over the central Indian Ocean (Lin et al. 2004).

The convective mass transport peaks in the lower troposphere, indicative of the preponderance of shallow convective-scale overturning (Fig. 4b). During the sup-pressed phase, the convective activity is comparatively
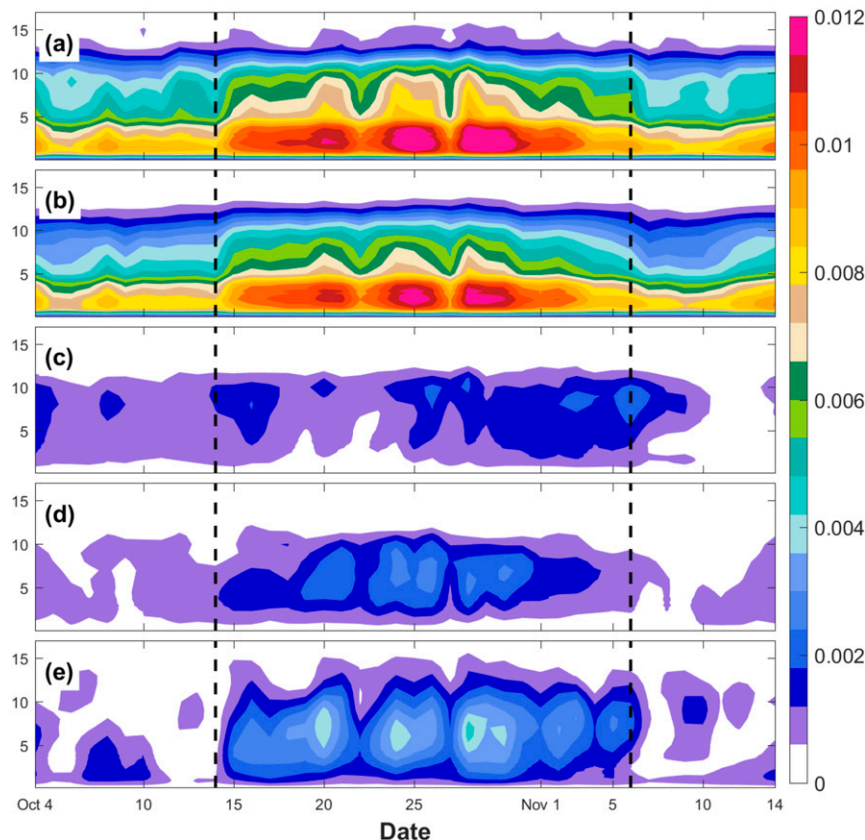
FIG. 4. Evolution of isentropic upward mass transports (color shading; $kg\,m^{-2}\,s^{-1}$) associated with (a) all scales, (b) convective scale, (c) regional scale, (d) meridional scale, and (e) basin scale averaged over 120 subregions. The black dashed lines show the onset and disrupted dates of the MJO event.

weak, especially above the freezing level. During the MJO active phase, the convective-scale overturning is reinforced considerably and becomes much deeper, with the strength of convective upward mass transport increases more than 50% in lower troposphere and reaches the strength around $0.5\,kg\,m^{-2}\,s^{-1}$ between 5- and 10-km altitude (Fig. 4b), which is consistent with Del Genio et al. (2012) and many other studies that found an enhancement of the tropical convective activity during the MJO. However, the convective overturning is still more prominent in the lower troposphere during the active phase, which indicates that both shallow and deep convection increase during the MJO active phase. The statistical significance of the differences in the convective-scale overturning for the active and suppressed MJO phases is tested using the t test. Results show that the increase in convective-scale overturning during the MJO active phase is statistically significant at the 99% confidence level.

The mass transports associated with the regional, meridional, and basin scales (Figs. 4c, 4d, and 4e) are one order of magnitude smaller than that associated with the mass transport by convective scale (Fig. 4b). The meridional and basinwide overturning also increase significantly during the MJO active phase (Figs. 4d and 4e; around 3 times stronger than the suppressed phase, statistically significant at the 99% confidence level), reflecting that the Hadley circulation is reinforced by the MJO heating; stronger basin-scale updraft is imposed by the lateral boundary (Fig. 4e). Similar to the analysis of the streamfunctions in Figs. 3c and 3d, both the meridional and basinwide upward mass transports peak at around 6 km, which considerably enhances the total upward mass transport in the middle troposphere ($\sim$34%) during the active phase of the MJO (Fig. 4a). In contrast, the contribution from the regional overturning to the mass transport shows a weak enhancement near the end of the MJO active phase but it is otherwise small (Fig. 4c). Several studies (e.g., Tromeur and Rossow 2010; Virts and Houze 2015) have pointed out the fact that the MJO corresponds to increased activity at the synoptic and mesoscales. However, such increases in
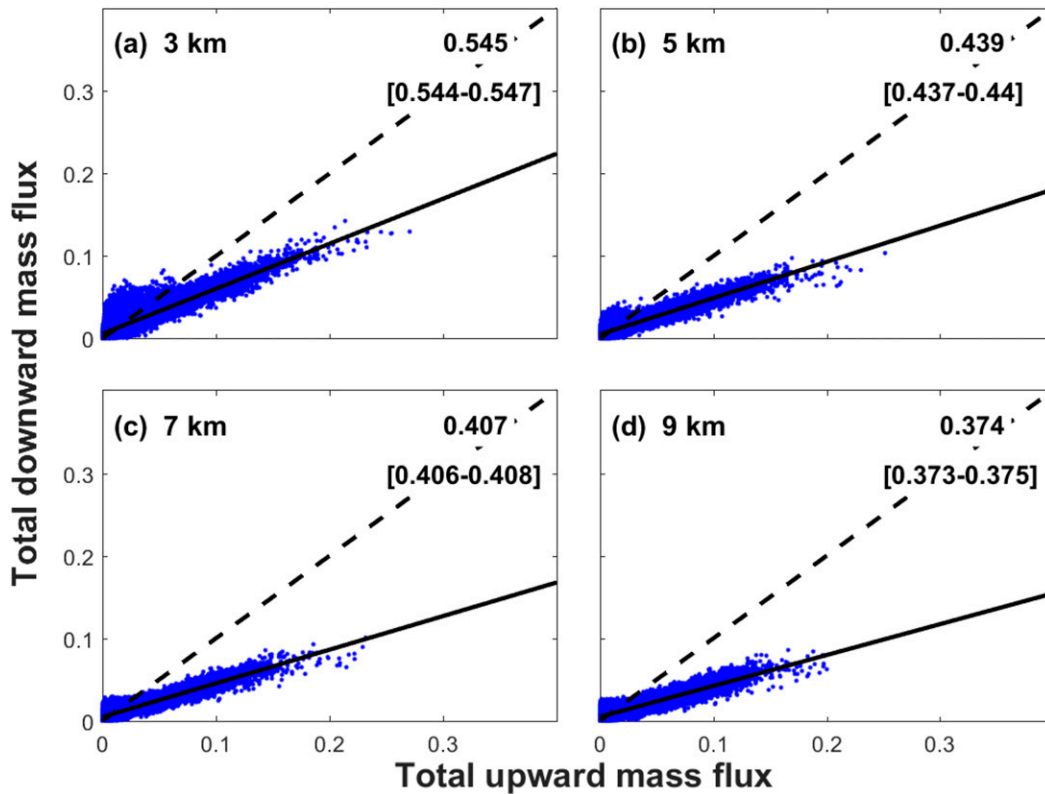
FIG. 5. Scatterplots of total upward vs downward mass fluxes ($kg\,m^{-2}\,s^{-1}$) at different altitudes over 120 subregions [from (a) 3 to (d) 9 km]. The black solid line in each panel represents the linear fit of the scatterplot. The linear regression coefficient and its 95% confidence interval are shown in the upper-right corner of each panel. The black dashed line in each panel shows a straight line with a slope of 1.0.

synoptic and mesoscale activity do not correspond to an increase in the atmospheric overturning. A possible explanation is that the isentropic analysis filters out the reversible oscillatory motions like gravity waves. For gravity waves, the ascending and subsiding motions are out of phase with the perturbations in both temperature and θ_e, so that their net contribution to the isentropic mass transport is small when averaged over the entire basin. Thus, if the mesoscale and synoptic-scale structures in the tropics fit the broader concept of convectively coupled gravity waves (Emanuel et al. 1994; Wheeler and Kiladis 1999), a majority of their contribution to the isentropic overturning will be filtered out and should be small when compared to other scales of motions, though the contribution from the nonlinear convectively coupled gravity waves with significant irreversible diabatic process cannot be purely removed by the isentropic analysis.

Figure 5 shows the scatterplots of total upward versus downward isentropic mass fluxes at different altitudes over all 120 subregions. The total upward (downward) mass fluxes shown here is the average of ascending (subsiding) air parcels at all equivalent potential temperatures

on different altitudes. We observe a strong correlation between the upward and downward mass fluxes, meaning that regions of strong updrafts are typically associated with stronger downdrafts. Note that the boundary conditions impose a large-scale ascent over the entire basin in the simulation (Fig. 3d), so that the upward mass flux is typically larger than the downward mass flux at all altitudes, and the linear regression coefficient between the two fluxes is smaller than 1.0 for the entire troposphere (Fig. 5). From a physical point of view, the ratio of the downward mass flux to the upward mass fluxes account for the ability of convective updrafts to generate convective downdrafts.

Figure 5 also shows that the ratio between the downward and upward mass fluxes decreases substantially with height. The linear regression coefficient between the downward and upward mass fluxes is high under the melting layer (0.545 at 3 km, with a 95% confidence interval from 0.544 to 0.547), showing that convective updrafts can generate a substantial amount of downdraft. The regression coefficient however decreases substantially above the freezing level, (0.374 at 9 km, with a 95% confidence interval from 0.373

to 0.375). This is consistent with the analysis of Fig. 4, which shows that convective mass transport peaks below the melting layer. The linear regression coefficient between the downward to upward mass flux can be physically interpreted in terms of the evaporation efficiency of the atmospheric overturning (Mrowiec et al. 2012). Thus, the isentropic analysis in our simulation is consistent with an evaporation efficiency of about 54% in the lower troposphere that gradually decreases to 37% in the upper troposphere. When compared to the tropic inland regions, for example sub-Saharan Africa (the evaporation efficiency is close to 1.0; Geerts and Dejene 2005), the evaporation efficiency in the MJO is much lower because of the moister large-scale environment over the tropic oceans.

As mentioned above, the direct contribution from the large scales (basin, meridional, and regional scales) to the total atmospheric overturning is one order of magnitude smaller than that from the convective activity. However, the large-scale flow can still essentially influence the total atmospheric overturning indirectly, since it provides the environment for the initiation and development of convection. To assess the convective-scale overturning under different large-scale regimes, we divide all convective-scale vertical mass transports into nine regimes based on the strength of $\overline{\rho}W_{LS}$ at 6-km altitude. The related isentropic streamfunctions of convective overturning in different regimes are shown in Fig. 6. The net large-scale vertical mass flux at 6 km is negative (subsiding regimes) for five cases (Figs. 6a–e) and positive (ascending regimes) for the last four cases (Figs. 6f–i).

In the subsiding regimes (Figs. 6a–e), the average strength of the convective overturning is weak. Convection is shallower and is dominated by warm-rain processes with its vertical circulation limited under the melting level. Though deep convective-scale ascent can still be found over the subsiding regimes, the strength is weak, reflecting that the large-scale subsidence suppresses the development of deep convective overturning. As mentioned above, the tilt of the streamfunction in the lower troposphere is closely related to the mixing between rising clouds and the environmental air, which results both in a reduction of θ_e inside clouds and in an increase of the θ_e in the environment. The tilt of the streamlines increases with the strength of the large-scale subsidence, which indicates that entrainment has a strong impact on the behavior of rising plumes (from Fig. 6e to Fig. 6a). Equivalent potential temperature θ_e of descending air parcels is also low in the subsidence regimes, with the lowest θ_e at about 317 K located at around 1.5 km. It should be noted that the spatial resolution of 9 km in our simulation is insufficient to accurately resolve the entrainment process. More pronounced entrainment should be expected in simulations with even higher spatial resolution.

In the ascending regimes (Figs. 6f–i), the convective overturning intensifies (5 times stronger than the convective overturning in the subsiding regimes on average). Shallow convective overturning is still prominent and an overturning mass transport peaks at around 1–4 km. Regions of large-scale ascent typically correspond to a moister (and slightly warmer) environment, which reduces the negative impacts of entrainment. This appears in the isentropic analysis as a reduction of the tilt of streamlines in the ascending regimes. The isentropic mass transport increases with the strength of the large-scale upward mass transport, which confirms that convective overturning is enhanced in regions of large-scale ascent. The isentropic mass transport is however systematically larger than the magnitude of the large-scale mass transport itself, which implies that convective motions tend to amplify the large-scale ascent.

To sum up, in comparison with the convective-scale circulation, the direct contribution from the large-scale circulations to the atmospheric overturning is relatively weak during the MJO event (Figs. 3 and 4). However, the large-scale circulations modulate the convective activity (Fig. 6). The large-scale upward motion and the associated low-level convergence and high-level divergence provide favorable atmospheric environment for the initiation and development of convective overturning. Similar results can also be found in the previous literatures (e.g., Johnson and Ciesielski 2013; Powell and Houze 2015; Ruppert and Johnson 2015). For example, in Powell and Houze (2015), they found that the large-scale circulation is instrumental to the onset of MJO events. In addition, large-scale motions appear to play a more substantial role in the isentropic mass transport in the middle to upper troposphere and may, thus, play a substantial role in increasing the depth of the atmospheric overturning.

4. Propagation of MJO as a convective envelope

As mentioned in the introduction, the MJO event is characterized as a large-scale envelope of enhanced convective activity which propagates eastward across the equatorial Indian and west Pacific Oceans at an average speed of $5\,\mathrm{m\,s^{-1}}$. In this section, the detailed spatial, vertical, and temporal variations of the convective-scale atmospheric overturning in the October MJO event will be investigated in the context of isentropic analysis, with a special emphasis on features associated with the MJO's eastward propagation.

a. Mass transport at different altitudes

Figure 7 shows the Hovmöller diagrams of the convective-scale isentropic upward mass transport (color shadings) and the mean vertical mass fluxes (black contours) averaged over subregions 61–75 at 2-, 5-, and 10-km
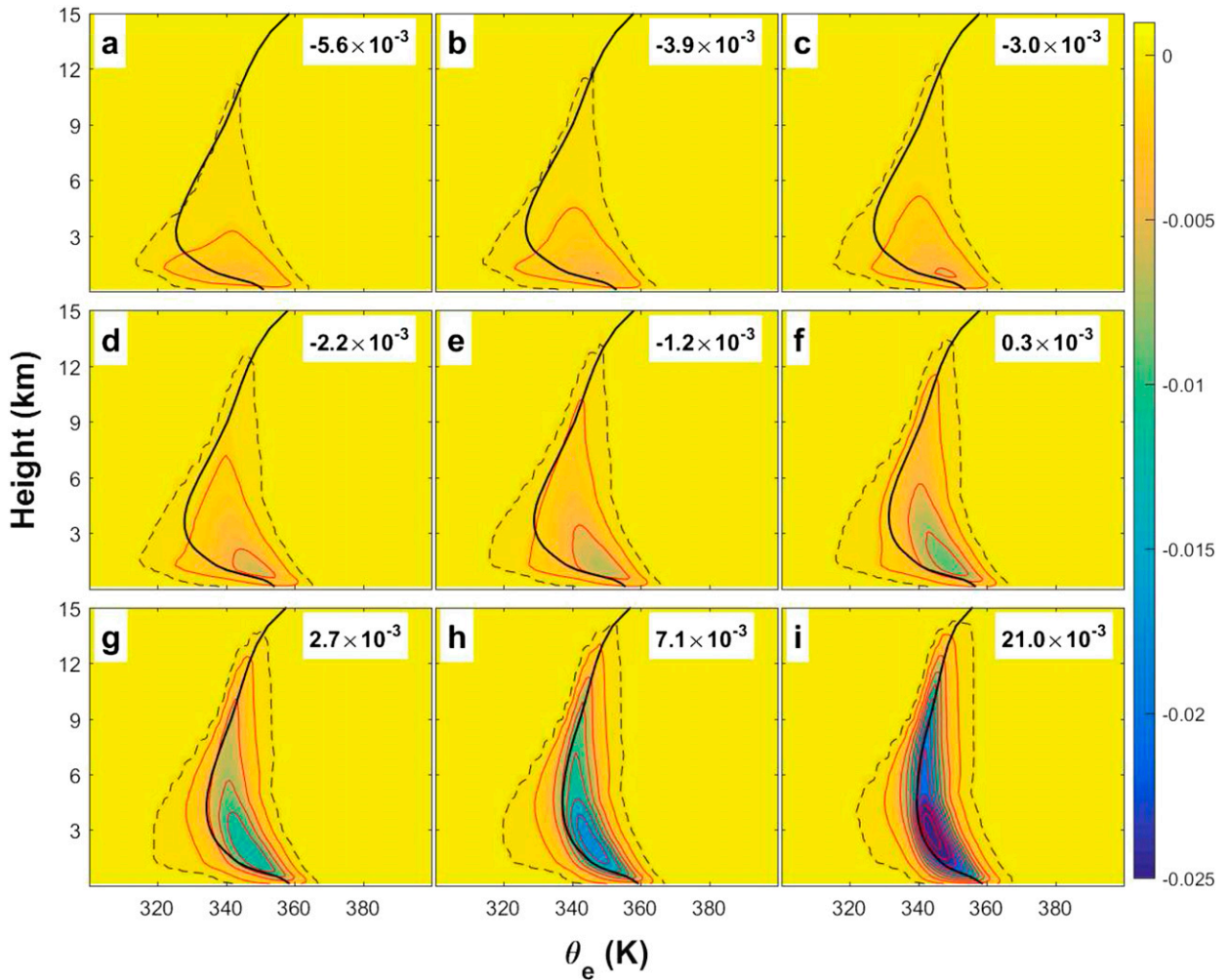
FIG. 6. Isentropic streamfunction (kg m^{-2} s^{-1}) of convective-scale overturning in different regimes of $\overline{\rho}W_{LS}$ strength (kg m^{-2} s^{-1}) at 6-km altitude [sorted by the strength of $\overline{\rho}W_{LS}$ at 6-km altitude; the mean strength of the 6-km $\overline{\rho}W_{LS}$ of the regime is shown in the upper-right corner of each panel]. The black solid line shows the mean profile of equivalent potential temperature in different regimes. Isolines of the streamfunctions are shown as red contours starting from -0.001 kg m^{-2} s^{-1} and with a -0.003 kg m^{-2} s^{-1} interval. The black dashed lines show the isolines of 0 kg m^{-2} s^{-1}.

altitudes, respectively. The x axis is the longitude (from the western equatorial Indian Ocean to the island of Borneo) and the y axis shows the dates. The onset and disrupted dates of the October MJO event are shown by the two white dashed lines. Both the convective-scale upward mass transports and the mean vertical mass fluxes are enhanced considerably after the onset of the MJO, indicating that the convective activity and the atmospheric overturning are enhanced during the active phase of this MJO event. The eastward propagation of the MJO is clearly captured by the convective-scale upward mass transports and the mean vertical mass fluxes at different levels. As for the surface rainfall field (Fig. 2), the eastward propagation of enhanced convective-scale upward mass transport is also disrupted near the Maritime

Continent (~100°E). During the active phase of the MJO event, the mean vertical mass flux is enhanced on the middle and upper troposphere (Figs. 7b and 7c), which is closely related to the strengthening of the basin- and meridional-scale atmospheric overturning during this period (Figs. 4d and 4e). Both shallow and deep convective-scale upward mass transports are enhanced during the MJO active phase (more than 50%, statistically significant at the 99% confidence level) while the mass transport in the lower troposphere is more prominent than that in the middle and upper troposphere (Figs. 7a–c). The enhancement of the deep convective-scale upward mass transport occurs simultaneously with the onset of the MJO, while the reinforcement of the shallow convective-scale upward mass transport occurs a few days earlier
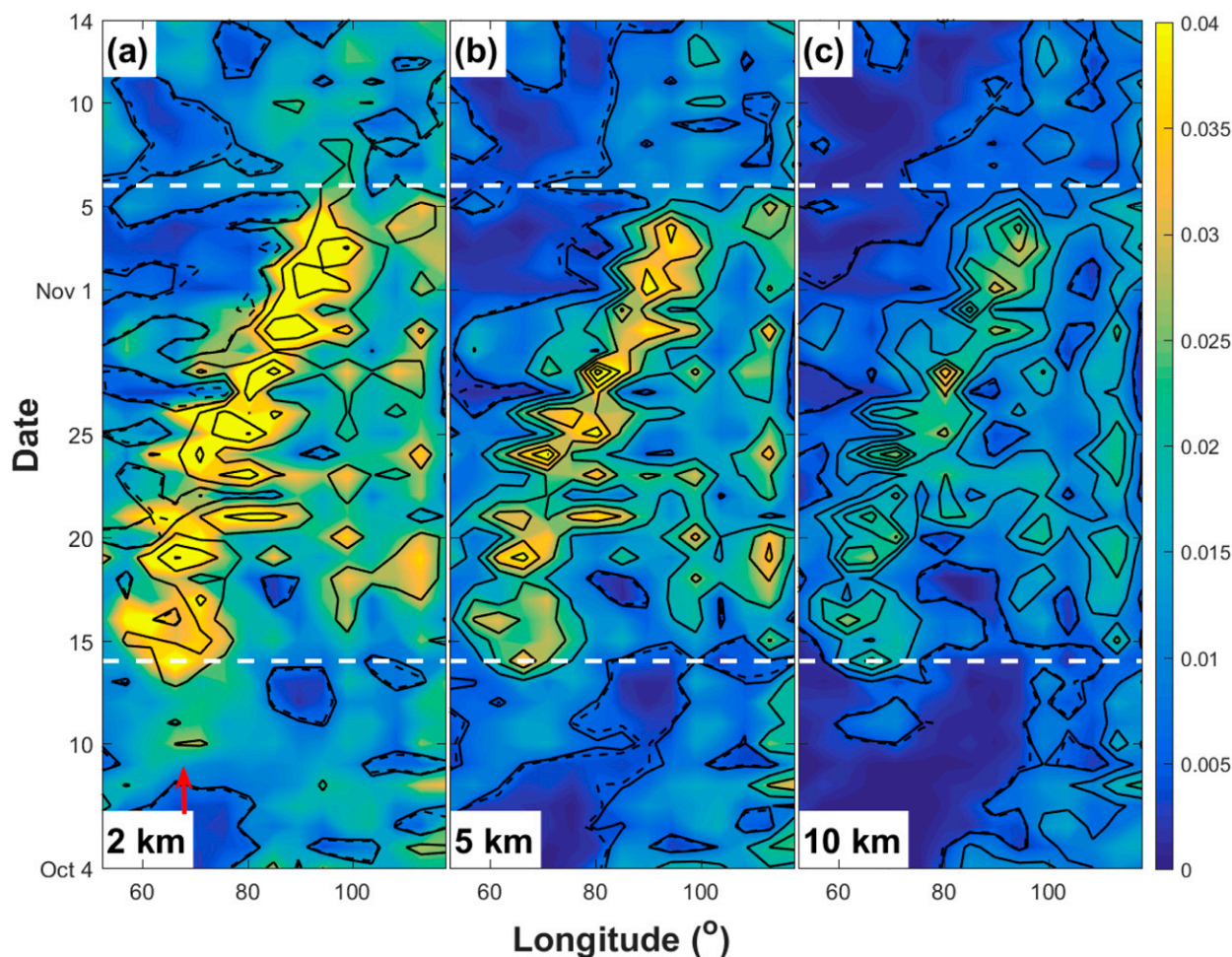
FIG. 7. Hovmöller diagrams of isentropic upward mass transport ($kg\,m^{-2}\,s^{-1}$) associated with the convective-scale (color shading) and mean mass flux (black contours; solid contours represent upward mean mass flux and dashed ones are downward mean mass flux; the interval is $1\,kg\,m^{-2}\,s^{-1}$) at (a) 2-, (b) 5-, and (c) 10-km altitudes. The white dashed lines show the onset and disrupted dates of the MJO event. The reinforcement of shallow upward mass transport is highlighted by the red arrow in (a).

(Figs. 7a and 7c). This strongly suggests that preconditioning by shallow congestus clouds might play an important role in the initial development of the MJO over the Indian Ocean. Previous studies show that preceding shallow or moderately deep convective activity can enhance the low-level mass convergence, moisten the lower troposphere, and produce a favorable environment for the initiation of deep convection (Zhang and Song 2009; Powell and Houze 2013; Chikira 2014; Xu and Rutledge 2014; Bellenger et al. 2015; Powell and Houze 2015; Ruppert and Johnson 2015; Takemi 2015; Powell 2016).

b. Mass flux in different subregions

The temporal and spatial evolutions of the vertical structure of convective-scale mass fluxes are further

investigated. Figure 8 presents the isentropic distributions of the convective-scale vertical mass fluxes averaged over different periods and subregions. As mentioned in section 3, the convective-scale atmospheric overturning is a combination of ascending air parcels with high potential temperature and descending air parcels at low potential temperature. For each subregion over the equatorial Indian Ocean (subregions 61–68), the convective-scale mass flux is weak (with the maximum vertical mass flux weaker than $0.003\,kg\,m^{-2}\,s^{-1}\,K^{-1}$) and shallow (below melting level) during the suppressed phase of the MJO event. While, during the active phase of the MJO event, it becomes much stronger (with the maximum vertical mass flux stronger than $0.008\,kg\,m^{-2}\,s^{-1}\,K^{-1}$) and deeper that connects the air from near the surface to the upper troposphere. The enhancements of the

convective-scale mass flux in all subregions during the active phase of the MJO are statistically significant at the 99% confidence level (the statistical significances are tested using the t test). Strong convective-scale mass fluxes are mainly concentrated in the lower troposphere which corresponds to the analysis of Figs. 3 and 4, indicating that shallow convective overturning dominates the mass transport in lower troposphere over the tropical Indian Ocean. The eastward propagation of the MJO event can be clearly captured by the strongest value of the convective-scale vertical mass flux in each equatorial subregion: from subregions 61–62 (15–19 October), to subregions 64–65 (20–24 October), to subregions 67–68 (25–29 October), and to subregions 70–71 (30 October–3 November), which corresponds to the eastward propagation of the convective-scale upward mass transports shown in Fig. 7. Because of the stronger convective heating, the environmental equivalent potential temperature also becomes higher in the lower and middle troposphere (shown by the black solid lines in Fig. 8) during the active phase of the MJO event. Over the Maritime Continent (subregions 74–75), the convective-scale mass flux, however, has been influenced little by the MJO event. The average rainfall rate in each subregion during different periods has also been given in Fig. 8, showing that the rainfall rate varies directly with the vertical convective-scale mass flux: a stronger convective activity produces stronger surface precipitation during the active phase of the MJO.

c. Vertical entropy transport

The isentropic analysis can also be used to assess the vertical transports of energy and entropy. As shown in Fig. 3a, on average, the potential temperature of ascending air parcels is higher than that of descending air parcels in the convective-scale overturning, which leads to an upward entropy transportation for the whole convective overturning.

One advantage of the isentropic analysis is it offers an efficient way to characterize the thermodynamic properties of the atmospheric overturning with the two-stream approximation (Pauluis and Mrowiec 2013). First, based on the convective-scale streamfunction averaged over the subregions 61–75, the convective-scale atmospheric overturning is divided into a mean updraft and a mean downdraft at each model output time. The upward M^+ and downward M^- mass transports are defined as

$$M^+(z,t) = \int_{-\infty}^{\infty} \langle \rho W_C \rangle H(\langle \rho W_C \rangle)\, d\theta_e \quad \text{and} \quad (11)$$

$$M^-(z,t) = \int_{-\infty}^{\infty} \langle \rho W_C \rangle H(-\langle \rho W \rangle_C)\, d\theta_e, \quad (12)$$

where z is altitude, t is the model integration time (output every hour), and H is a Heaviside step function.

In the convective-scale atmospheric overturning, M^+ and M^- cancel each other out in the absence of mean vertical motion. The isentropic-mean equivalent potential temperatures in the mean updraft θ_e^+ and in the mean downdraft θ_e^- are defined as

$$\theta_e^+(z,t) = \frac{1}{M^+} \int_{-\infty}^{\infty} \langle \rho W_C \theta_e \rangle H(\langle \rho W_C \rangle)\, d\theta_e' \quad \text{and} \quad (13)$$

$$\theta_e^-(z,t) = \frac{1}{M^-} \int_{-\infty}^{\infty} \langle \rho W_C \theta_e \rangle H(-\langle \rho W_C \rangle)\, d\theta_e'. \quad (14)$$

The temporal evolutions of the isentropic-mean equivalent potential temperature perturbation in the mean convective-scale updraft $[\theta_e^+(z,t) - \overline{\theta_e^+}(z)]$ and downdraft $[\theta_e^-(z,t) - \overline{\theta_e^-}(z)]$ are shown in the Figs. 9a and 9b. Over the equatorial Indian Ocean, the equivalent potential temperature in the convective updraft becomes ~4 K higher in the troposphere during the active phase of the MJO (statistically significant at the 99% confidence level), which corresponds to greater latent heat released by the anomalous convective activity during this period (Fig. 9a). The equivalent potential temperature perturbation in the mean convective-scale updraft is fairly uniform with height below the tropopause during the active phase of the MJO (0.5~1.0 K). This indicates that the updrafts transmit fairly efficiently and uniformly the variations of equivalent potential temperature from the surface to the entire troposphere. Above the tropopause, the equivalent potential temperature decreases during the active phase of the MJO. One possible explanation is that it pointing to the presence of stronger convective overshooting, which is associated with a weak downward entropy transport as rising air mixes with air parcels of higher equivalent potential temperature before subsiding. Another possible reason is that it is induced by the vertically propagating Kelvin waves excited by the MJO convective envelope (Johnson and Ciesielski 2013). The exact mechanisms still need future investigations.

The evolution of equivalent potential temperature of the mean downdraft θ_e^- shows a different structure than that of the mean updraft. First, θ_e^- decreases in the boundary layer during the active phase of the MJO (statistically significant at the 99% confidence level), which is likely due to stronger convective downdrafts bringing more air parcels with low equivalent potential temperature from the free atmosphere into the boundary layer. The stronger cold pools (Feng et al. 2015; Rowe and Houze 2015; Skyllingstad and de Szoeke 2015) may also play a role in the formation of the boundary layer negative equivalent potential temperature anomaly during the active phase of the MJO. Second, in the lower troposphere (but above the mixed layer), θ_e^- is increased
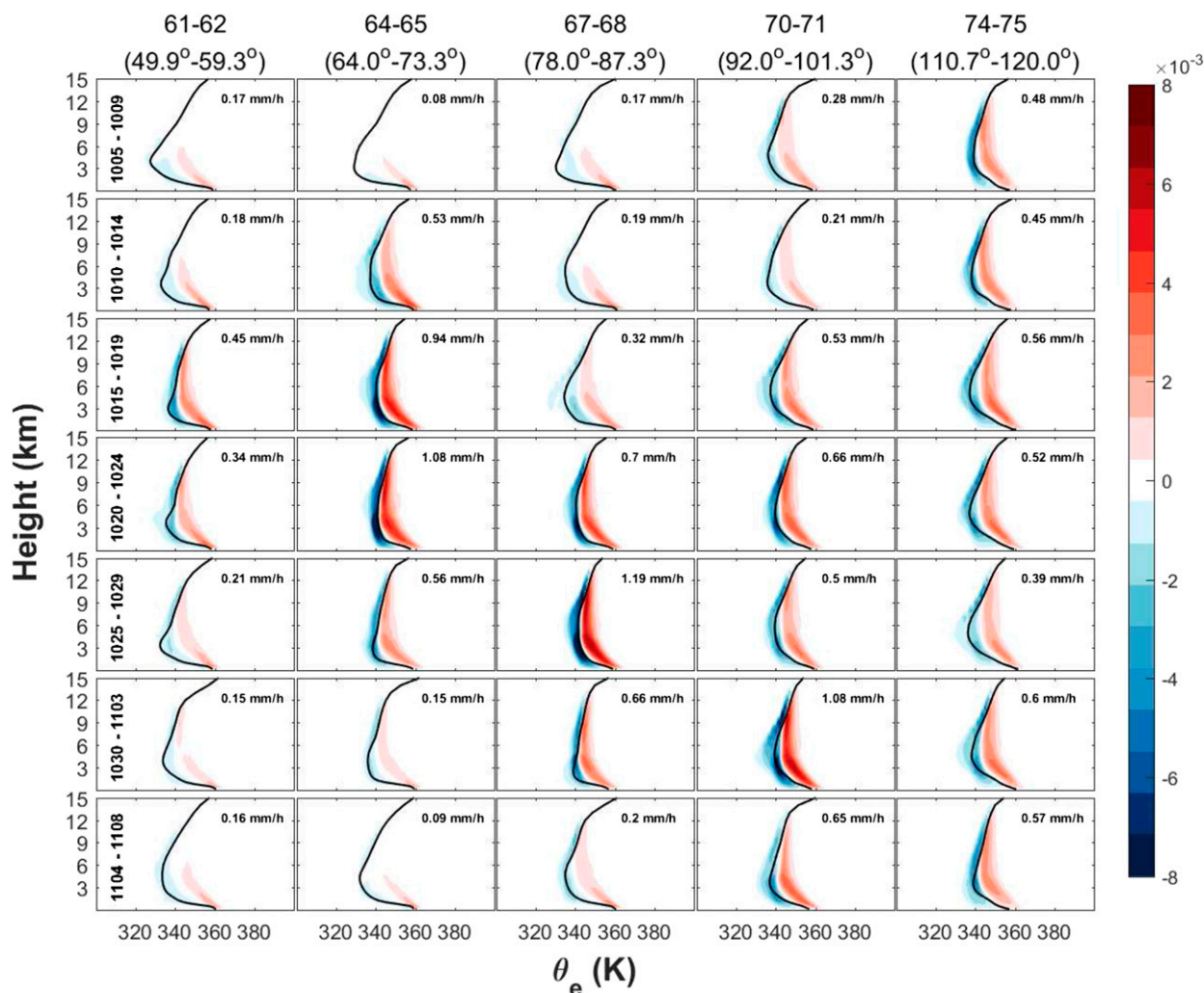
FIG. 8. Isentropic distributions of convective-scale vertical mass flux (kg m^{-2} s^{-1} K^{-1}; color shading) averaged over different subregions (columns) and different periods (rows). For each panel, the x axis is equivalent potential temperature (K) and the y axis is height (km). The black solid line shows the mean profile of equivalent potential temperature. The mean surface rain rate over the subregion is shown in the upper-right corner of each panel. The number of subregions and their longitude ranges are shown at the top of each column. Time period (month day–month day) is shown in each panel of the first column.

by 5 K at the onset of the MJO (statistically significant at the 99% confidence level), corresponding to a moistening of the lower troposphere. Though the equivalent potential temperature increased both in the convective updraft and downdraft during the transition from the MJO suppressed phase to active phase, this change is much less significant when compared with the variation of other strong tropic atmospheric systems, like hurricane (Mrowiec et al. 2016).

The evolution of isentropic-mean equivalent potential temperature differences between the mean convective-scale updraft and downdraft is shown in Fig. 9c. As mentioned before, rising air parcels have higher equivalent potential temperature than the subsiding air parcels on average, indicating that there has an upward

entropy transport in the convective-scale atmospheric overturning. The equivalent potential temperature differences between the mean updraft and downdraft decreases with the height and changes sign near the tropopause. The entropy transport by convection is upward through the troposphere and reverses direction near the tropopause. The equivalent potential temperature differences between the mean updraft and downdraft become smaller in the lower troposphere during the active phase of the MJO event, which reflects a moister environment. The largest difference in equivalent potential temperature between updraft and downdraft is about 15 K which occurs between 5 and 10 October. This difference gradually decreases before the onset reaching its lowest value of about 10 K
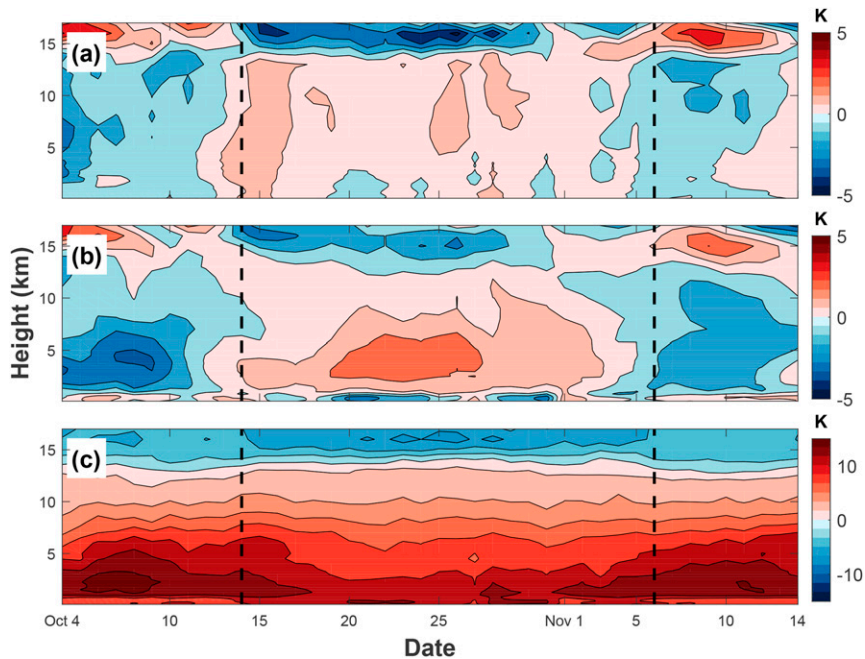
FIG. 9. (a) Evolution of perturbation isentropic-mean equivalent potential temperature (K) in the mean convective-scale updraft. (b) As in (a), but for the mean convective-scale downdraft. (c) Evolution of the isentropic-mean equivalent potential temperature difference (K) between the mean convective-scale updraft and downdraft $[\theta_e^+(z, t) - \theta_e^-(z, t)]$. The onset and disrupted dates of the MJO event are shown by the black dashed lines.

between 20 and 25 October. The active phase of the MJO thus corresponds to a period of reduced thermodynamic difference between updraft and downdraft. This means that convection is less efficient at reducing the equivalent potential temperature of the lower troposphere, so that more convective mass transport is necessary to compensate for a given surface heating.

5. Summary and discussion

In this study, we analyze the atmospheric overturning across multiple scales during the October MJO event observed by the CINDY/DYNAMO campaign. The MJO event is simulated with the WRF Model under the same configuration as W15. Isentropic analysis proposed by Pauluis and Mrowiec (2013) is applied in this study, for the first time for such a purpose, to investigate the contributions of individual scales to the total atmospheric overturning of the MJO. The framework of isentropic analysis analyzes the atmospheric overturning by conditionally averaging vertical mass transport in terms of the equivalent potential temperature and describes the flow in a height–entropy (z–θ_e) coordinate. This approach makes it possible to unambiguously extract the mass transport associated with different scales in the high-resolution simulation.

The overturning circulation of the MJO event is decomposed into four contributions: a basinwide ascent (basin scale), a zonally symmetric meridional overturning (meridional scale), zonal asymmetries on scales larger than 450 km (regional scale), and a convective contribution associated with all scales less than 450 km (convective scale). Our analysis shows that the atmospheric overturning over the Indian Ocean is dominated by the contribution from the convective scale. The overturning associated with other scales of motion is at least one order magnitude smaller than that owing to convection. However, the vertical mass transport by the convective scale peaks in the lower troposphere, while the transport by the larger scales reaches its maximum in the midtroposphere. This indicates that while the atmospheric overturning is dominated by the smaller scales, the larger scales enable the atmospheric overturning to reach a higher altitude than it would owing to the influence of convection alone.

We also analyze the evolution of the upward mass transport. During the active phase of the MJO, the atmospheric overturning associated with all scales becomes significantly stronger. This increase of mass transport is most pronounced for the contributions from the convective scales. The large-scale overturning is also important because it can significantly enhance the

vertical mass transport in the middle to upper tropo-sphere and modulate the convective activity. Notably, the convective mass transport intensifies in the lower troposphere a few days before the initiation of the MJO event. This strongly indicates that preconditioning by shallow congestus clouds plays an important role in the development of the MJO over the Indian Ocean.

In contrast to the previous studies based on coarse-resolution models or large-scale atmospheric datasets that do not resolve the convective scale and only capture the atmospheric overturning by the large-scale atmo-spheric motion (e.g., Kiladis et al. 2005; Johnson and Ciesielski 2013), the isentropic analysis based on cloud-permitting simulation shows that convective scale dominates the atmospheric overturning of the MJO and strongly interacts with the large scales. The contribution of convective scale to the total atmospheric overturning is much larger in the isentropic analysis than that in the traditional Eulerian averaging, because the condi-tional averaging based on equivalent temperature can better extract the vertical mass flux associated with convective scale.

The eastward propagation of the MJO is clearly cap-tured by the eastward propagation of the convective-scale vertical mass transport. Prior to initiation of the MJO, there is a noticeable increase in shallow convec-tive overturning in the equatorial Indian Ocean. The initiation itself corresponds to the intensification and deepening of convection which then slowly propagates eastward. The convective-scale vertical mass trans-port over the Maritime Continent, however, has been influenced little by the MJO event. In our simulation, the MJO propagation can be unequivocally identified from the propagation of the convective mass transport, without applying any additional filtering which is usually needed to be done for the precipitation or OLR fields.

Isentropic analysis also offers an efficient way to di-vide the upward and downward mass transports in the convective-scale overturning and characterize the ther-modynamic properties of convective-scale updraft and downdraft separately. The convective-scale vertical en-tropy transport in the MJO event has been studied in this paper. In the mean convective-scale updraft, the averaged equivalent potential temperature becomes higher in the troposphere while lower above the tropo-pause during the active phase of the MJO, which is re-lated to stronger and deeper convective activity during this period. Similar evolution can also be found in the mean convective-scale downdraft. In the boundary layer, the averaged equivalent potential temperature is decreased in the mean convective-scale downdraft during the active phase of the MJO, which is related to

the stronger convective downdraft and cold pools. In general, the increase of equivalent potential tempera-ture of convective-scale overturning during the MJO active phase is not significant, especially when compared to the variations of other strong tropic atmospheric systems like hurricane (Mrowiec et al. 2016).

With the isentropic analysis technique, detailed ther-modynamic cycles and energy transport of multiscale atmospheric overturning in the MJO can also be in-vestigated based on the mean airflow as Lagrangian dynamics approximation (Pauluis 2016), which would be interesting to study in the future. Using cloud-resolving models with parameterized large-scale dynamics, sev-eral recent studies have investigated the interactions between convection development and large-scale over-turning in the tropics (e.g., Wang et al. 2013, 2016). These modeling results are also deserving of further analysis using the isentropic analysis technique.

REFERENCES

Barnes, H. C., and R. A. Houze, 2014: Precipitation hydrometeor type relative to the mesoscale airflow in mature oceanic deep convection of the Madden-Julian Oscillation. *J. Geophys. Res. Atmos.*, **119**, 13 990–914 014, https://doi.org/10.1002/2014JD022241.

Bellenger, H., K. Yoneyama, M. Katsumata, T. Nishizawa, K. Yasunaga, and R. Shirooka, 2015: Observation of moisture tendencies related to shallow convection. *J. Atmos. Sci.*, **72**, 641–659, https://doi.org/10.1175/JAS-D-14-0042.1.

Bergman, J. W., H. H. Hendon, and K. M. Weickmann, 2001: Intra-seasonal air–sea interactions at the onset of El Niño. *J. Climate*, **14**, 1702–1719, https://doi.org/10.1175/1520-0442(2001)014<1702:IASIAT>2.0.CO;2.

Chen, N., A. J. Majda, and D. Giannakis, 2014: Predicting the cloud patterns of the Madden-Julian Oscillation through a low-order nonlinear stochastic model. *Geophys. Res. Lett.*, **41**, 5612–5619, https://doi.org/10.1002/2014GL060876.

Chi, Y., F. Zhang, W. Li, J. He, and Z. Guan, 2015: Correlation between the onset of the East Asian subtropical summer monsoon and the eastward propagation of the Madden–Julian oscillation. *J. Atmos. Sci.*, **72**, 1200–1214, https://doi.org/10.1175/JAS-D-14-0038.1.

Chikira, M., 2014: Eastward-propagating intraseasonal oscillation represented by Chikira–Sugiyama cumulus parameterization. Part II: Understanding moisture variation under weak tem-perature gradient balance. *J. Atmos. Sci.*, **71**, 615–639, https://doi.org/10.1175/JAS-D-13-038.1.

Dee, D. P., and Coauthors, 2011: The ERA-Interim reanalysis: Configuration and performance of the data assimilation system. *Quart. J. Roy. Meteor. Soc.*, **137**, 553–597, https://doi.org/10.1002/qj.828.

Del Genio, A. D., Y. Chen, D. Kim, and M.-S. Yao, 2012: The MJO transition from shallow to deep convection in *CloudSat/CALIPSO* data and GISS GCM simulations. *J. Climate*, **25**, 3755–3770, https://doi.org/10.1175/JCLI-D-11-00384.1.

DePasquale, A., C. Schumacher, and A. Rapp, 2014: Radar observations of MJO and Kelvin wave interactions during DYNAMO/CINDY2011/AMIE. *J. Geophys. Res. Atmos.*, **119**, 6347–6367, https://doi.org/10.1002/2013JD021031.

Emanuel, K. A., 1994: *Atmospheric Convection.* Oxford University Press, 592 pp.

——, J. David Neelin, and C. S. Bretherton, 1994: On large-scale circulations in convecting atmospheres. *Quart. J. Roy. Meteor. Soc.*, **120**, 1111–1143, https://doi.org/10.1002/qj.49712051902.

Feng, Z., S. Hagos, A. K. Rowe, C. D. Burleyson, M. N. Martini, and S. P. de Szoeke, 2015: Mechanisms of convective cloud organization by cold pools over tropical warm ocean during the AMIE/DYNAMO field campaign. *J. Adv. Model. Earth Syst.*, **7**, 357–381, https://doi.org/10.1002/2014MS000384.

Fu, X., J.-Y. Lee, P.-C. Hsu, H. Taniguchi, B. Wang, W. Wang, and S. Weaver, 2013: Multi-model MJO forecasting during DYNAMO/CINDY period. *Climate Dyn.*, **41**, 1067–1081, https://doi.org/10.1007/s00382-013-1859-9.

Geerts, B., and T. Dejene, 2005: Regional and diurnal variability of the vertical structure of precipitation systems in Africa based on spaceborne radar data. *J. Climate*, **18**, 893–916, https://doi.org/10.1175/JCLI-3316.1.

Hagos, S. M., Z. Feng, C. D. Burleyson, C. Zhao, M. N. Martini, and L. K. Berg, 2016: Moist process biases in simulations of the Madden–Julian oscillation episodes observed during the AMIE/DYNAMO field campaign. *J. Climate*, **29**, 1091–1107, https://doi.org/10.1175/JCLI-D-15-0349.1.

He, J., H. Lin, and Z. Wu, 2011: Another look at influences of the Madden-Julian Oscillation on the wintertime East Asian weather. *J. Geophys. Res.*, **116**, D03109, https://doi.org/10.1029/2010JD014787.

Hendon, H. H., and B. Liebmann, 1994: Organization of convection within the Madden-Julian oscillation. *J. Geophys. Res.*, **99**, 8073–8083, https://doi.org/10.1029/94JD00045.

Hong, S.-Y., Y. Noh, and J. Dudhia, 2006: A new vertical diffusion package with an explicit treatment of entrainment processes. *Mon. Wea. Rev.*, **134**, 2318–2341, https://doi.org/10.1175/MWR3199.1.

Hung, M.-P., J.-L. Lin, W. Wang, D. Kim, T. Shinoda, and S. J. Weaver, 2013: MJO and convectively coupled equatorial waves simulated by CMIP5 climate models. *J. Climate*, **26**, 6185–6214, https://doi.org/10.1175/JCLI-D-12-00541.1.

Iacono, M. J., J. S. Delamere, E. J. Mlawer, M. W. Shephard, S. A. Clough, and W. D. Collins, 2008: Radiative forcing by long-lived greenhouse gases: Calculations with the AER radiative transfer models. *J. Geophys. Res.*, **113**, D13103, doi:10.1029/2008JD009944.

Janiga, M. A., and C. Zhang, 2016: MJO moisture budget during DYNAMO in a cloud-resolving model. *J. Atmos. Sci.*, **73**, 2257–2278, https://doi.org/10.1175/JAS-D-14-0379.1.

Jiang, X., and Coauthors, 2015: Vertical structure and physical processes of the Madden-Julian oscillation: Exploring key model physics in climate simulations. *J. Geophys. Res. Atmos.*, **120**, 4718–4748, https://doi.org/10.1002/2014JD022375.

Johnson, R. H., and P. E. Ciesielski, 2013: Structure and properties of Madden–Julian oscillations deduced from DYNAMO sounding arrays. *J. Atmos. Sci.*, **70**, 3157–3179, https://doi.org/10.1175/JAS-D-13-065.1.

Kerns, B. W., and S. S. Chen, 2014: ECMWF and GFS model forecast verification during DYNAMO: Multiscale variability in MJO initiation over the equatorial Indian Ocean. *J. Geophys. Res. Atmos.*, **119**, 3736–3755, https://doi.org/10.1002/2013JD020833.

Kiladis, G. N., K. H. Straub, and P. T. Haertel, 2005: Zonal and vertical structure of the Madden–Julian oscillation. *J. Atmos. Sci.*, **62**, 2790–2809, https://doi.org/10.1175/JAS3520.1.

Klemp, J. B., J. Dudhia, and A. D. Hassiotis, 2008: An upper gravity-wave absorbing layer for NWP applications. *Mon. Wea. Rev.*, **136**, 3987–4004, https://doi.org/10.1175/2008MWR2596.1.

Klotzbach, P. J., 2014: The Madden–Julian oscillation's impacts on worldwide tropical cyclone activity. *J. Climate*, **27**, 2317–2330, https://doi.org/10.1175/JCLI-D-13-00483.1.

Lim, K.-S. S., and S.-Y. Hong, 2010: Development of an effective double-moment cloud microphysics scheme with prognostic cloud condensation nuclei (CCN) for weather and climate models. *Mon. Wea. Rev.*, **138**, 1587–1612, https://doi.org/10.1175/2009MWR2968.1.

Lin, J., B. Mapes, M. Zhang, and M. Newman, 2004: Stratiform precipitation, vertical heating profiles, and the Madden–Julian oscillation. *J. Atmos. Sci.*, **61**, 296–309, https://doi.org/10.1175/1520-0469(2004)061<0296:SPVHPA>2.0.CO;2.

——, and Coauthors, 2006: Tropical intraseasonal variability in 14 IPCC AR4 climate models. Part I: Convective signals. *J. Climate*, **19**, 2665–2690, https://doi.org/10.1175/JCLI3735.1.

Ling, J., P. Bauer, P. Bechtold, A. Beljaars, R. Forbes, F. Vitart, M. Ulate, and C. Zhang, 2014: Global versus local MJO forecast skill of the ECMWF model during DYNAMO. *Mon. Wea. Rev.*, **142**, 2228–2247, https://doi.org/10.1175/MWR-D-13-00292.1.

Liu, C., E. J. Zipser, D. J. Cecil, S. W. Nesbitt, and S. Sherwood, 2008: A cloud and precipitation feature database from nine years of TRMM observations. *J. Appl. Meteor. Climatol.*, **47**, 2712–2728, https://doi.org/10.1175/2008JAMC1890.1.

Lorenz, D. J., and D. L. Hartmann, 2006: The effect of the MJO on the North American monsoon. *J. Climate*, **19**, 333–343, https://doi.org/10.1175/JCLI3684.1.

Madden, R. A., and P. R. Julian, 1971: Detection of a 40–50 day oscillation in the zonal wind in the tropical Pacific. *J. Atmos. Sci.*, **28**, 702–708, https://doi.org/10.1175/1520-0469(1971)028<0702:DOADOI>2.0.CO;2.

Majda, A. J., and J. A. Biello, 2004: A multiscale model for tropical intraseasonal oscillations. *Proc. Natl. Acad. Sci. USA*, **101**, 4736–4741, https://doi.org/10.1073/pnas.0401034101.

——, S. N. Stechmann, and B. Khouider, 2007: Madden-Julian Oscillation analog and intraseasonal variability in a multi-cloud model above the equator. *Proc. Natl. Acad. Sci. USA*, **104**, 9919–9924, https://doi.org/10.1073/pnas.0703572104.

Maloney, E. D., and D. L. Hartmann, 2001: The Madden–Julian oscillation, barotropic dynamics, and North Pacific tropical cyclone formation. Part I: Observations. *J. Atmos. Sci.*, **58**, 2545–2558, https://doi.org/10.1175/1520-0469(2001)058<2545:TMJOBD>2.0.CO;2.

Moum, J. N., and Coauthors, 2014: Air–sea interactions from westerly wind bursts during the November 2011 MJO in the Indian Ocean. *Bull. Amer. Meteor. Soc.*, **95**, 1185–1199, https://doi.org/10.1175/BAMS-D-12-00225.1.

Mrowiec, A. A., C. Rio, A. M. Fridlind, A. S. Ackerman, A. D. Del Genio, O. M. Pauluis, A. C. Varble, and J. Fan, 2012: Analysis of cloud-resolving simulations of a tropical mesoscale convective system observed during TWP-ICE: Vertical fluxes and draft properties in convective and stratiform regions. *J. Geophys. Res.*, **117**, D19201, doi:10.1029/2012JD017759.

——, O. M. Pauluis, A. M. Fridlind, and A. S. Ackerman, 2015: Properties of a mesoscale convective system in the context of an isentropic analysis. *J. Atmos. Sci.*, **72**, 1945–1962, https://doi.org/10.1175/JAS-D-14-0139.1.

——, ——, and F. Zhang, 2016: Isentropic analysis of a simulated hurricane. *J. Atmos. Sci.*, **73**, 1857–1870, https://doi.org/10.1175/JAS-D-15-0063.1.

Pai, D. S., J. Bhate, O. P. Sreejith, and H. R. Hatwar, 2011: Impact of MJO on the intraseasonal variation of summer monsoon rainfall over India. *Climate Dyn.*, **36**, 41–55, https://doi.org/10.1007/s00382-009-0634-4.

Pauluis, O., 2016: The mean air flow as Lagrangian dynamics approximation and its application to moist convection. *J. Atmos. Sci.*, **73**, 4407–4425, https://doi.org/10.1175/JAS-D-15-0284.1.

——, and A. A. Mrowiec, 2013: Isentropic analysis of convective motions. *J. Atmos. Sci.*, **70**, 3673–3688, https://doi.org/10.1175/JAS-D-12-0205.1.

——, A. Czaja, and R. Korty, 2008: The global atmospheric circulation on moist isentropes. *Science*, **321**, 1075–1078, https://doi.org/10.1126/science.1159649.

——, ——, and ——, 2010: The global atmospheric circulation in moist isentropic coordinates. *J. Climate*, **23**, 3077–3093, https://doi.org/10.1175/2009JCLI2789.1.

Pilon, R., C. Zhang, and J. Dudhia, 2016: Roles of deep and shallow convection and microphysics in the MJO simulated by the model for prediction across scales. *J. Geophys. Res. Atmos.*, **121**, 10 575–510 600, https://doi.org/10.1002/2015JD024697.

Powell, S. W., 2016: Updraft buoyancy within and moistening by cumulonimbi prior to MJO convective onset in a regional model. *J. Atmos. Sci.*, **73**, 2913–2934, https://doi.org/10.1175/JAS-D-15-0326.1.

——, and R. A. Houze, 2013: The cloud population and onset of the Madden-Julian Oscillation over the Indian Ocean during DYNAMO-AMIE. *J. Geophys. Res. Atmos.*, **118**, 11 979–911 995, https://doi.org/10.1002/2013JD020421.

——, and ——, 2015: Effect of dry large-scale vertical motions on initial MJO convective onset. *J. Geophys. Res. Atmos.*, **120**, 4783–4805, https://doi.org/10.1002/2014JD022961.

Rowe, A. K., and R. A. Houze, 2014: Microphysical characteristics of MJO convection over the Indian Ocean during DYNAMO. *J. Geophys. Res. Atmos.*, **119**, 2543–2554, https://doi.org/10.1002/2013JD020799.

——, and ——, 2015: Cloud organization and growth during the transition from suppressed to active MJO conditions. *J. Geophys. Res. Atmos.*, **120**, 10 324–310 350, https://doi.org/10.1002/2014JD022948.

Ruppert, J. H., and R. H. Johnson, 2015: Diurnally modulated cumulus moistening in the preonset stage of the Madden–Julian oscillation during DYNAMO. *J. Atmos. Sci.*, **72**, 1622–1647, https://doi.org/10.1175/JAS-D-14-0218.1.

Shi, J. J., and Coauthors, 2010: WRF simulations of the 20–22 January 2007 snow events over eastern Canada: Comparison with in situ and satellite observations. *J. Appl. Meteor. Climatol.*, **49**, 2246–2266, https://doi.org/10.1175/2010JAMC2282.1.

Skamarock, W. C., and Coauthors, 2008: A description of the Advanced Research WRF version 3. NCAR Tech. Note NCAR/TN-475+STR, 113 pp., http://dx.doi.org/10.5065/D68S4MVH.

Skyllingstad, E. D., and S. P. de Szoeke, 2015: Cloud-resolving large-eddy simulation of tropical convective development and surface fluxes. *Mon. Wea. Rev.*, **143**, 2441–2458, https://doi.org/10.1175/MWR-D-14-00247.1.

Slawinska, J., O. Pauluis, A. J. Majda, and W. W. Grabowski, 2016: Multiscale interactions in an idealized Walker cell: Analysis with isentropic streamfunctions. *J. Atmos. Sci.*, **73**, 1187–1203, https://doi.org/10.1175/JAS-D-15-0070.1.

Slingo, J. M., and Coauthors, 1996: Intraseasonal oscillations in 15 atmospheric general circulation models: Results from an AMIP diagnostic subproject. *Climate Dyn.*, **12**, 325–357, https://doi.org/10.1007/BF00231106.

Sobel, A., S. Wang, and D. Kim, 2014: Moist static energy budget of the MJO during DYNAMO. *J. Atmos. Sci.*, **71**, 4276–4291, https://doi.org/10.1175/JAS-D-14-0052.1.

Takemi, T., 2015: Relationship between cumulus activity and environmental moisture during the CINDY2011/DYNAMO field experiment as revealed from convection-resolving simulations. *J. Meteor. Soc. Japan*, **93A**, 41–58, https://doi.org/10.2151/jmsj.2015-035.

Tewari, M., and Coauthors, 2004: Implementation and verification of the unified Noah land surface model in the WRF model. *20th Conf. on Weather Analysis and Forecasting/16th Conf. on Numerical Weather Prediction*, Seattle, WA, Amer. Meteor. Soc., 14.2a, https://ams.confex.com/ams/84Annual/techprogram/paper_69061.htm.

Tromeur, E., and W. B. Rossow, 2010: Interaction of tropical deep convection with the large-scale circulation in the MJO. *J. Climate*, **23**, 1837–1853, https://doi.org/10.1175/2009JCLI3240.1.

Tyrrell, G. C., D. J. Karoly, and J. L. McBride, 1996: Links between tropical convection and variations of the extratropical circulation during TOGA COARE. *J. Atmos. Sci.*, **53**, 2735–2748, https://doi.org/10.1175/1520-0469(1996)053<2735:LBTCAV>2.0.CO;2.

Virts, K. S., and R. A. Houze, 2015: Variation of lightning and convective rain fraction in mesoscale convective systems of the MJO. *J. Atmos. Sci.*, **72**, 1932–1944, https://doi.org/10.1175/JAS-D-14-0201.1.

Wang, S., A. H. Sobel, and Z. Kuang, 2013: Cloud-resolving simulation of TOGA-COARE using parameterized large-scale dynamics. *J. Geophys. Res. Atmos.*, **118**, 6290–6301, https://doi.org/10.1002/jgrd.50510.

——, ——, F. Zhang, Y. Q. Sun, Y. Yue, and L. Zhou, 2015: Regional simulation of the October and November MJO events observed during the CINDY/DYNAMO field campaign at gray zone resolution. *J. Climate*, **28**, 2097–2119, https://doi.org/10.1175/JCLI-D-14-00294.1.

——, ——, and J. Nie, 2016: Modeling the MJO in a cloud-resolving model with parameterized large-scale dynamics: Vertical structure, radiation, and horizontal advection of dry air. *J. Adv. Model. Earth Syst.*, **8**, 121–139, https://doi.org/10.1002/2015MS000529.

Wang, W., A. Kumar, J. X. Fu, and M.-P. Hung, 2015: What is the role of the sea surface temperature uncertainty in the prediction of tropical convection associated with the MJO? *Mon. Wea. Rev.*, **143**, 3156–3175, https://doi.org/10.1175/MWR-D-14-00385.1.

Wheeler, M., and G. N. Kiladis, 1999: Convectively coupled equatorial waves: Analysis of clouds and temperature in the wavenumber–frequency domain. *J. Atmos. Sci.*, **56**, 374–399, https://doi.org/10.1175/1520-0469(1999)056<0374:CCEWAO>2.0.CO;2.

Xiang, B., M. Zhao, X. Jiang, S.-J. Lin, T. Li, X. Fu, and G. Vecchi, 2015: The 3–4-week MJO prediction skill in a GFDL coupled model. *J. Climate*, **28**, 5351–5364, https://doi.org/10.1175/JCLI-D-15-0102.1.

Xu, W., and S. A. Rutledge, 2014: Convective characteristics of the Madden–Julian oscillation over the central Indian Ocean observed by shipborne radar during DYNAMO. *J. Atmos. Sci.*, **71**, 2859–2877, https://doi.org/10.1175/JAS-D-13-0372.1.

Yamada, R., and O. Pauluis, 2016: Momentum balance and Eliassen–Palm flux on moist isentropic surfaces. *J. Atmos. Sci.*, **73**, 1293–1314, https://doi.org/10.1175/JAS-D-15-0229.1.

Yoneyama, K., C. Zhang, and C. N. Long, 2013: Tracking pulses of the Madden–Julian oscillation. *Bull. Amer. Meteor. Soc.*, **94**, 1871–1891, https://doi.org/10.1175/BAMS-D-12-00157.1.

Zhang, C., 2005: Madden-Julian Oscillation. *Rev. Geophys.*, **43**, RG2003, https://doi.org/10.1029/2004RG000158.

——, J. Gottschalck, E. D. Maloney, M. W. Moncrieff, F. Vitart, D. E. Waliser, B. Wang, and M. C. Wheeler, 2013: Cracking the MJO nut. *Geophys. Res. Lett.*, **40**, 1223–1230, https://doi.org/10.1002/grl.50244.

Zhang, G. J., and X. Song, 2009: Interaction of deep and shallow convection is key to Madden-Julian Oscillation simulation. *Geophys. Res. Lett.*, **36**, L09708, https://doi.org/10.1029/2009GL037340.

Zuluaga, M. D., and R. A. Houze, 2013: Evolution of the population of precipitating convective systems over the equatorial Indian Ocean in active phases of the Madden–Julian oscillation. *J. Atmos. Sci.*, **70**, 2713–2725, https://doi.org/10.1175/JAS-D-12-0311.1.